HKUST-1 Metal-Organic Framework Nanoparticle/Graphene Oxide Nanocomposite Aerogels for CO_2 and CH_4 Adsorption and Separation

Albert Rosado,[1] Alejandro Borrás,[1] Julio Fraile,[1] Jorge A. R. Navarro,[2] Fabián Suárez-García,[3] Kyriakos C. Stylianou,[4] Ana M. López-Periago,[1] José Giner Planas,[1,*] Concepción Domingo,[1,*] Amirali Yazdi[1,*]

Author Information:

Albert Rosado: Materials Science Institute of Barcelona, ICMAB-CSIC, Campus UAB s/n, 08193, Barcelon, Spain. Email: arosado@icmab.es

Alejandro Borrás: Instituto de Ciencia de Materiales de Barcelona, ICMAB-CSIC, Campus UAB s/n, 08193, Barcelon, Spain. Email: aborras@icmab.es

Julio Fraile: Instituto de Ciencia de Materiales de Barcelona, ICMAB-CSIC, Campus UAB s/n, 08193, Barcelon, Spain. Email: julio@icmab.es

Jorge A. R. Navarro: Departamento de Química Inorgánica, Universidad de Granada, Av. Fuentenueva S/N, 18071, Granada, Spain. Email: jarn@ugr.es

Fabián Suárez-García: Instituto de Ciencia y Tecnología del Carbono, INCAR-CSIC, C/Francisco Pintado Fe 26, 33011, Oviedo, Spain. Email: fabian@incar.csic.es

Kyriakos C. Stylianou: Department of Chemistry, Oregon State University, Corvallis, OR 97331, USA kyriakos.stylianou@oregonstate.edu

Ana M. López-Periago: Instituto de Ciencia de Materiales de Barcelona, ICMAB-CSIC, Campus UAB s/n, 08193, Barcelon, Spain. Email: amlopez@icmab.es

José Giner Planas: Instituto de Ciencia de Materiales de Barcelona, ICMAB-CSIC, Campus UAB s/n, 08193, Barcelon, Spain. Email: jginerplanas@icmab.es. Corresponding author

Concepción Domingo: Instituto de Ciencia de Materiales de Barcelona, ICMAB-CSIC, Campus UAB s/n, 08193, Barcelon, Spain. Email: conchi@icmab.es. Corresponding author

Amirali Yazdi: Instituto de Ciencia de Materiales de Barcelona, ICMAB-CSIC, Campus UAB s/n, 08193, Barcelon, Spain. Email: amirali.yazdi@yahoo.com. Corresponding author

KEYWORDS: Supercritical CO_2, composite materials, HKUST-1/GO, aerogels, gas adsorption, gas separation.

Abstract

The development of nanostructured composites made of metal-organic frameworks (MOFs) and graphene-based components, including exfoliated nanoplates of graphene oxide (GO) or reduced (rGO) graphene oxide, is an area of great interest in gas storage and separation. To improve the industrial viability, it is commonly demanded to build these nanocomposites with the shape of compact units, such as monoliths, foams, pellets or films. Methods to generate those 3D nanocomposites involving rGO are abundant; however, they become scarce when GO is the desired support due to the difficulty in maintaining the carbon matrix oxidized during the structuration process. In this work, a methodology based on the use of supercritical CO_2 ($scCO_2$) is described for the synthesis of nanocomposites involving a discontinuous MOF phase, *e.g.* nanoparticles (NPs) of HKUST-1, decorating the surface of a continuous GO matrix, with surface oxygen groups favoring MOF attachment. The use of this new supercritical methodology allows the nanostructuration of the composite in the form of 3D aerogels, while avoiding the reduction of GO. Enhanced values of textural properties, determined by low-temperature N_2 adsorption-desorption, were observed for the nanocomposites in comparison to the values calculated for similar physical mixtures, highlighting an increase of 40-45 % in the value of surface area for samples with high percentage of HKUST-1. Moreover, the composite aerogels, displaying a type II isotherm, outperform pristine HKUST-1 in regard of CH_4 practical working capacity at high pressure. Particularly, a composite exhibiting more than 2-fold the working capacity of net HKUST-1 NPs was obtained. Columns involving the composite aerogel as the stationary phase were used to study the separation of N_2/CO_2 and CH_4/CO_2 gas mixtures. The results showed a high selectivity of the nanostructured HKUST-1@GO composites for CO_2, with breakthrough times of *ca.* 20 $ming^{-1}$ and stable cyclic operation.

1. Introduction

For high-technology applications, the processing of powders, specially nanopowders, into useful objects such as nanostructured monoliths, foams, pellets or films, becomes essential in various sectors, not only due to better performance, but also due to issues related to easy handling of nano-objects and worker's safety.[1] In this respect, nanoporous non-particulate sorbents are being developed to replace the traditional beds of powder or granules in order to solve the drawbacks of flow maldistribution, channeling, high pressure drop and mass transfer resistance, particularly when high throughputs are required, as well as in cyclic processes to increase kinetics and, thus, production.[2,3] Graphene-based nanomaterials, including activated carbon, nanotubes, or graphene and its oxidized analogs graphene oxide (GO) and reduced graphene oxide (rGO), are some of the most studied matrixes in nanostructured adsorbents, which have been widely used in the sorption of hazardous materials and for the photocatalytic degradation of pollutants in water remediation, as well as for the physisorption and chemisorption in processes of separation of gases.[4] Most of the advantageous properties found in these sorbents can be improved by building them as nanocomposite materials to achieve more sophisticated characteristics and, thereby, to increase their usability by integrating the unique properties of composing nano-units. Particularly, the category of composites made of metal-organic frameworks (MOFs) and GO has received tremendous attention in the past years.[5,6,7] On one hand, the nanoporous MOFs family is one of the most promising class of solid materials selected, together with zeolites, for gas storage and separation.[8,9,10] On the other hand, GO is an easily processable nanomaterial with numerous surface oxygen groups favoring MOF attachment.

First reported GO/MOFs composites were hydrothermally synthesized by epitaxial growth,[11] and they are described as constituted by a matrix of MOF microcrystals with

intercalated rGO nanosheets.[12,13] More recently, composites involving a discontinuous MOF phase, usually nanoparticles (NPs), decorating the surface of a continuous rGO matrix have been described.[14] These hybrids can be obtained either by the solvothermal *in situ* crystallization of the MOF in the presence of dispersed GO flakes or by the *ex situ* physical mixing of pre-synthesized components. When a 3D structuration of the composite affording aerogels is pursued, the formation of a gel-derived precursor is required previous to the drying process. The gel is generally obtained following a hydro/solvothermal approach which inevitably leads to GO reduction.[15] Only a few examples of non-reduced MOF/GO aerogel composites have been reported, obtained by freeze-drying as very fragile foams.[16,17] Although much research has been devoted to the development of GO/MOFs nanostructured adsorbents in the last decade, there is still a need to design new methods that avoid harsh chemicals and/or elevated temperatures during synthesis, thus obtaining nanocomposites of highly exfoliated and oxidized GO.

The best way to maintain GO exfoliated in a dry product is through the formation of highly porous aerogels,[15] which can be constructed by using a low-temperature supercritical carbon dioxide ($scCO_2$) method to induce gelation,[18] as it was demonstrated in our laboratories.[19,20] The method is also able to produce robust nanocomposites involving non-reduced GO. This promising technique is here extended to the synthesis of low-density MOF@GO composite aerogels by adapting the $scCO_2$ protocol to *ex situ* and *in situ* methods. Particularly, HKUST-1 was chosen as the case study to exemplify the method possibilities. Indeed, the attractive functionality of nanoporous HKUST-1, one of the few commercially marketed MOFs,[21] has already spurred significant efforts directed toward their combination with carbon-based materials for gas sorption applications.[22,23]

This work also intends to increase the understanding of the advantages of nanostructuring the HKUST-1@GO adsorbent into a 3D aerogel for gas adsorption in batch and under flow in semi-continuous separation processes. The category of composites combining HKUST-1 and graphene, mainly rGO, has previously been exploited to engineer new and beneficial pore structures targeted to the adsorption and separation of small gas molecules, *e.g.*, CO_2 and nitrogen (N_2),[24] methane (CH_4),[25] and hydrogen (H_2),[26] and for gas separation (CH_4/CO_2 and N_2/CO_2).[27] The design of new sorbent structures must involve a trade-off between chemical and textural characteristics, *e.g.*, macroscopic 3D structure, stability, composition, morphology, surface area or pore volume and nanoscopic pore topology, which would govern the overall sorbent performance, *e.g.*, uptake, kinetics, mass transfer or diffusion paths and selectivity. Accordingly, this study explores the influence of some experimental parameters (synthesis method, processing conditions and components ratio) on the sorption properties of the end materials. The static adsorption of CH_4 at high pressure was also measured, since HKUST-1 has been proposed as a microporous material for natural gas storage.[28] Actually, comparable structures to the aerogels prepared in this work, *i.e.*, foams, with inherent large porosity and high surface area values, have been shown to be capable of maintaining enhanced adsorption kinetics due to high surface area values and lower pressure drop than compacted pellets.[2,29] Hence, the prepared systems were also tested as the stationary phase for dynamic gas separation of N_2/CO_2 and CH_4/CO_2.

2. Materials and methods

2.1. Materials

GO nanosheets were purchased from Graphenea Inc. (Spain), supplied as a stable dispersion in water with a concentration of 4 $mgmL^{-1}$. For the preparation of microporous NPs of HKUST-1

($Cu_3(BTC)_2$), the used reagents were copper nitrate hydrate ($Cu(NO_3)_2 \cdot 3H_2O$, Panreac), benzene-1,3,5-tricarboxylic acid (H_3BTC, Sigma-Aldrich) and sodium acetate (NaAc, Carlo Erba). N,N-dimethylformamide (DMF), ethanol (EtOH), and methanol (MeOH) were the used liquid solvents provided by Acros Organics, Scharlau, and Panreac, respectively. Compressed CO_2 (99.95 wt%) for synthesis and gasses for adsorption (N_2, CO_2 and CH_4, 99.995 wt%) were all delivered by Carburos Metálicos S.A.

2.2. Preparation methods

Nanocomposite samples were prepared starting from a long-term stable colloidal suspension of GO nanoflakes in MeOH with a concentration of 4 $mgmL^{-1}$, which was obtained from the commercial GO dispersion in water by following a multi-step water-to-methanol exchange procedure described elsewhere.[19] Aerogel nanocomposites involving HKUST-1 NPs decorating GO flakes were prepared based on the use of $scCO_2$ by either an *ex situ* or *in situ* technique (Fig. S1). Relevant experimental parameters are summarized in Table 1.

Table 1. Experimental procedures used to obtain the different samples.

Sample	Precursor	Added GO:HK [wt%]	Drying treatment
GO_{sc}	GO in MeOH	100:0	
*ex*_HK_{sc}	HK NPs in MeOH	0:100	
*in*_HK_{sc}	$Cu(NO_3)_2$ + BTC + NaAc in MeOH	0:100	
*ex*_A_{sc}	GO in MeOH + HK NPs	50:50	$scCO_2$ 20 MPa 333 K
*ex*_B_{sc}		25:75	
*ex*_C_{sc}		10:90	
*in*_C_{sc}	GO in MeOH + $Cu(NO_3)_2$ + BTC + NaAc	10:90	
*ex*_C_{ad}	GO in MeOH + HK NPs	10:90	air RT

2.2.1. *Ex situ* preparation of HKUST-1@GO nanocomposite precursor dispersions

The *ex situ* method consists in integrating pre-synthesized HKUST-1 NPs (HK) with composing GO flakes by direct mixing in MeOH (Fig. S1a). For this, nanosized crystals of HKUST-1 were first precipitated employing a previously described method based on the addition of an excess of an alkaline salt (NaAc), used as a crystal growth modulator agent.[30] Briefly, 1.04 g of $Cu(NO_3)_2 \cdot 3H_2O$ (4.3 mmol) and 0.50 g of BTC (2.4 mmol) were dissolved separately in two aliquots of 12 mL of a 1:1:1 solvent mixture of DMF:H_2O:EtOH. Both solutions were then mixed in a 50 mL vial and 5 equivalents of NaAc, with respect to BTC, were added. The mixture was vigorously shaken. The vial was closed and placed into an electrical oven at 353 K for 24 h. After cooling, a blue suspension was collected, which was sonicated/centrifuged (x2 in 25 mL MeOH). After the last centrifugation step, the solid was re-dispersed in 50 mL of MeOH and left stirring at 500 rpm overnight. Following, the solid was washed again by sonication/centrifugation (x2 in 25

mL MeOH). Finally, the centrifuged solid was dried under soft vacuum at room temperature. The sky-blue as-synthesized HKUST-1 was activated under high vacuum (10 Pa) at 433 K during 20 h, becoming purple. The precursor dispersions for the *ex situ* composites were obtained by sonication of different amounts of HK NPs (20, 60, or 180 mg) added to aliquots of 5 mL of a GO dispersion in MeOH, corresponding to mixtures of 50:50, 25:75, and 10:90 wt% for GO:HKUST-1. Moreover, 180 mg of bare HK NPs were dispersed in 5 mL of MeOH free of GO to obtain the precursor of an *ex situ* sample of bare HKUST-1.

2.2.2. *In situ* preparation of HKUST-1@GO nanocomposite precursor dispersions

The *in situ* method involves the growth of HKUST-1 NPs from a system containing dissolved reagents and dispersed GO (Fig. S1b). For this purpose, a weighted amount of $Cu(NO_3)_2 \cdot 3H_2O$ (260 mg) was added to 5 mL of GO dispersion in MeOH and sonicated for 10 min. Then, 125 mg of BTC were added to the vial and the mixture was again sonicated for 10 min. Afterward, excess of NaAc was provided and sonication continued for 20 min. The obtained suspensions were sonicated/centrifuged until the supernatant lost the bluish appearance and became transparent (x4 in 15 mL MeOH). Finally, each precipitate was re-dispersed in 5 mL of fresh MeOH by sonication. The amount of reagents was calculated to have a GO:HKUST-1 weight percentage of 10:90 wt%. The same procedure, but without GO, was followed to obtain the precursor of an *in situ* sample of bare HKUST-1.

2.2.3. $scCO_2$ treatment for aerogel formation

Three assay tubes of 2 mL were loaded with aliquots of 1 mL of each previously prepared precursor dispersion in MeOH. Each set of three vials was placed into a 200 mL high-pressure reactor for $scCO_2$ drying. Liquid CO_2 was flushed into the vessel at 6 MPa and then heated at 333 K. The pressure was increased up to 20 MPa by adding compressed CO_2. These conditions were

maintained for 48 h. Afterwards, the reactor was slowly depressurized to atmospheric pressure under isothermal conditions (333 K) and, finally, cooled down to room temperature. Recovered samples were denoted with the suffix "sc" (Table 1). For bare materials, powder of *ex*_HK_{sc}, fragile aerogels of *in*_HK_{sc} and stable cylindrical blocks of GO_{sc} were recovered. For composites, always dry robust aerogel cylinders were obtained, named as *ex*_A_{sc}, *ex*_B_{sc} and *ex*_C_{sc} for the *ex situ* 50:50, 25:75 and 10:90 wt% GO:HKUST-1 ratios, and *in*_C_{sc} for the *in situ* 10:90 wt% GO:HKUST-1 ratio. The recovered aerogel samples were stored under vacuum in a desiccator for further characterization in an attempt to reduce the fast atmospheric water adsorption of HKUST-1 NPs.

For comparison, aliquots of 2 mL of the *ex situ* precursor dispersion of *ex*_C_{sc}, with concentration 10:90 wt% for GO:HKUST-1, were placed in an open glass vial and left to dry at RT to obtain an air dried (denoted with the suffix "ad") sample (*ex*_C_{ad}) (Table 1).

2.3. Characterization

2.3.1. Composition, structure, and morphology

The percentage of HKUST-1 in the prepared nanocomposites was determined through the Cu atomic ratio measured by inductively coupled plasma mass spectrometry (ICP-MS, Agilent 7700x) after solids digestion in hydrochloric and nitric acids. Weight of main components in the composites, as well as thermal stability, were assessed through thermogravimetric analysis in air flow (TGA, Netzsch-STA 449 F1 Jupiter) using a temperature increase step of 5 $Kmin^{-1}$. The structure of the composing materials and the composites was characterized by routine powder X-ray diffraction (XRD) in a Siemens D-5000 diffractometer with Cu Kα radiation. The molecular arrangement was investigated using Fourier transform infrared (FTIR) spectroscopy (Jasco 4700 Spectrophotometer) using the attenuated total reflection (ATR) accessory. The morphological

features were examined by using scanning electron microscopy (SEM, Quanta FEI 200). C, O, and Cu distribution were assessed by energy dispersive spectroscopy (EDS) in a high-resolution SEM microscope (FEI Magellan 400L, Ultim Extreme Oxford Inst.), placing the sample on a holder of silicon wafer and metalizing with Pd/Au. For the nanoparticulate systems, histograms of particle size distribution were obtained by measuring *ca.* 200 discrete particles in images taken with a transmission electron microscope (TEM, JEOL 1210) by using the ImageJ program.

2.3.2. Textural properties and adsorptive behavior

The textural properties were determined by N_2 adsorption/desorption at 77 K using an ASAP 2020 Micromeritics Inc. equipment. Previous to measurement, samples were outgassed under reduced pressure at 353 K during 20 h. The routine (post-)equilibrium time interval between points measurement was of 10 s, although in some experiments this time was increased to 120 s to study sorption kinetics. The specific surface area (Sa) was calculated by applying the BET (Brunauer, Emmet, Teller) equation, while the micropore volume (μPv) and apparent micropore surface area (μSa) were determined by the t-plot method. The nanopore volumetric size distribution was analyzed following two different methods: (i) the micropore (< 2 nm diameter) was estimated by the Dubinin-Astakhov (DA) method extracting information from the low pressure region of the isotherms (p/p^0 between 0.001 and 0.13), and (ii) the mesopore (> 2 nm - *ca.* 50 nm diameter) was calculated at the intermediate part of the isotherm using the BJH (Barrett, Joyner and Halenda) method based on the Kelvin equation.[31]

N_2, CO_2 and CH_4 adsorptions at 273 K and 0.1 MPa were also studied using the same equipment and the activation procedure described previously. Selected samples were cycled up to five times in regard of N_2 adsorption at 77 K to test the structural and sorption stability of prepared materials. Moreover, CO_2 adsorption isotherms were measured up to 0.1 MPa at 273, 298 and 313 K to

calculate the isosteric heat of adsorption (Q_{st}), determined through the graphical representation of the pressure logarithm (lnp) for a given adsorbed amount (n) as a function of the reciprocal temperature (1/T). The Q_{st} at a specific adsorbate loading was then estimated using the Clausius-Clapeyron equation (1):[32]

$$Q_{st}(n) = -R \ln (p_2/p_1) (T_1T_2/(T_2-T_1)) \quad (1)$$

Nanocomposing materials and nanocomposites were tested for CH_4 high-pressure adsorption up to 10 MPa at 298 K in a high-pressure volumetric sorption apparatus (iSorp HP Quantachrome). The samples were degassed *in situ* at 353 K under high vacuum for 10 h. The bulk gas amounts were calculated by using the Schmidt-Wenzel type equation of state, defined in terms of Helmholtz free energy (National Institute of Standards and Technology -NIST- recommended). The experimentally measured data was obtained as excess gravimetric uptake (N_{exc}), which was transformed into absolute gravimetric uptake, also called total uptake (N_{tu}), by using equation (2):

$$N_{tu}(p,T) = N_{exc}(p,T) + \rho(p,T) \cdot Pv \quad (2)$$

where ρ is the density of the gas at a certain pressure and temperature, obtained from NIST data files, and Pv is the single point total pore volume determined through the BET equation. For net HKUST-1, the used Pv corresponds to the μPv.

Dynamic breakthrough tests were performed using stainless steel fixed-bed columns (0.7 x 7 cm diameter x length) by using aerogels straightforwardly growth inside the column. Gas separation of N_2/CO_2 and CH_4/CO_2 at atmospheric pressure and 273 K was studied in the home-made semi-continuous system shown in Fig. S2. He gasses (2 $mLmin^{-1}$) at 353 K was used as a tracer during the experiments for the regeneration of the aerogels, as well as for purging and cleaning the lines of the adsorption system. In a typical test, a flow of CO_2, diluted with either N_2 or CH_4 in a volume ratio of 15:85 v%, was pumped through the column at 0.1 MPa with a total

inlet flow rate of 10 $mLmin^{-1}$. Relative amounts of gases passing through the fixed bed were monitored with a mass spectrometer gas analysis system (Pfeiffer Vacuum) detecting ion peaks at m/z 44 (CO_2), 14 (N_2), 16 (CH_4) and 4 (He). Selected samples were measured in regard of cycling stability up to five times. Based on the breakthrough curves, the adsorption capacity (q_i) of each gas was calculated in [$mmolg^{-1}$] as follows (3):

$$q_i = (Q \cdot x_i \cdot t_i) / 22.4 \qquad (3)$$

where Q is the flow rate, x_i is the feeding molar fraction of gas i at STP and t is the breakthrough time of gas i normalized by gram of adsorbent. With that, the separation selectivity α_{ij} could be calculated using equation (4):[33]

$$\alpha_{ij} = (q_i/x_i) / (q_j/x_j) \qquad (4)$$

3. Results and discussion

3.1. HKUST-1@GO synthesis, composition, morphology and nanostructure

Nanocomposite precursor dispersions were treated under $scCO_2$ at mild conditions (20 MPa and 333 K), by either direct mixing of both nanoentities, involving the *ex situ* synthesis of HK NPs (*ex*_HK@GO, Fig. S1a), or by the *in situ* growth of HKUST-1 in the presence of GO (*in*_HK@GO, Fig. S1b). Reference *ex*_HK_{sc} and *in*_HK_{sc} products were obtained by processing exclusively the HK precursors (Table 1). The recovered pristine *ex*_HK_{sc} sample was a nanopowder (Fig. 1a) with a mean diameter of 41 ± 11 nm measured from TEM images (Fig. 1b). Sample *in*_HK_{sc} was recovered as a brittle aerogel, which was inevitably pulverized during manipulation. The *in*_HK_{sc} NPs, with a mean size of 32 ± 8 nm (Fig. 1c,d), were significantly smaller than those obtained by the *ex situ* method. GO_{sc} aerogel displayed a sponge-like nanoporous (meso/macro) structure of multiple exfoliated GO nanosheets (Fig. 1e,f).

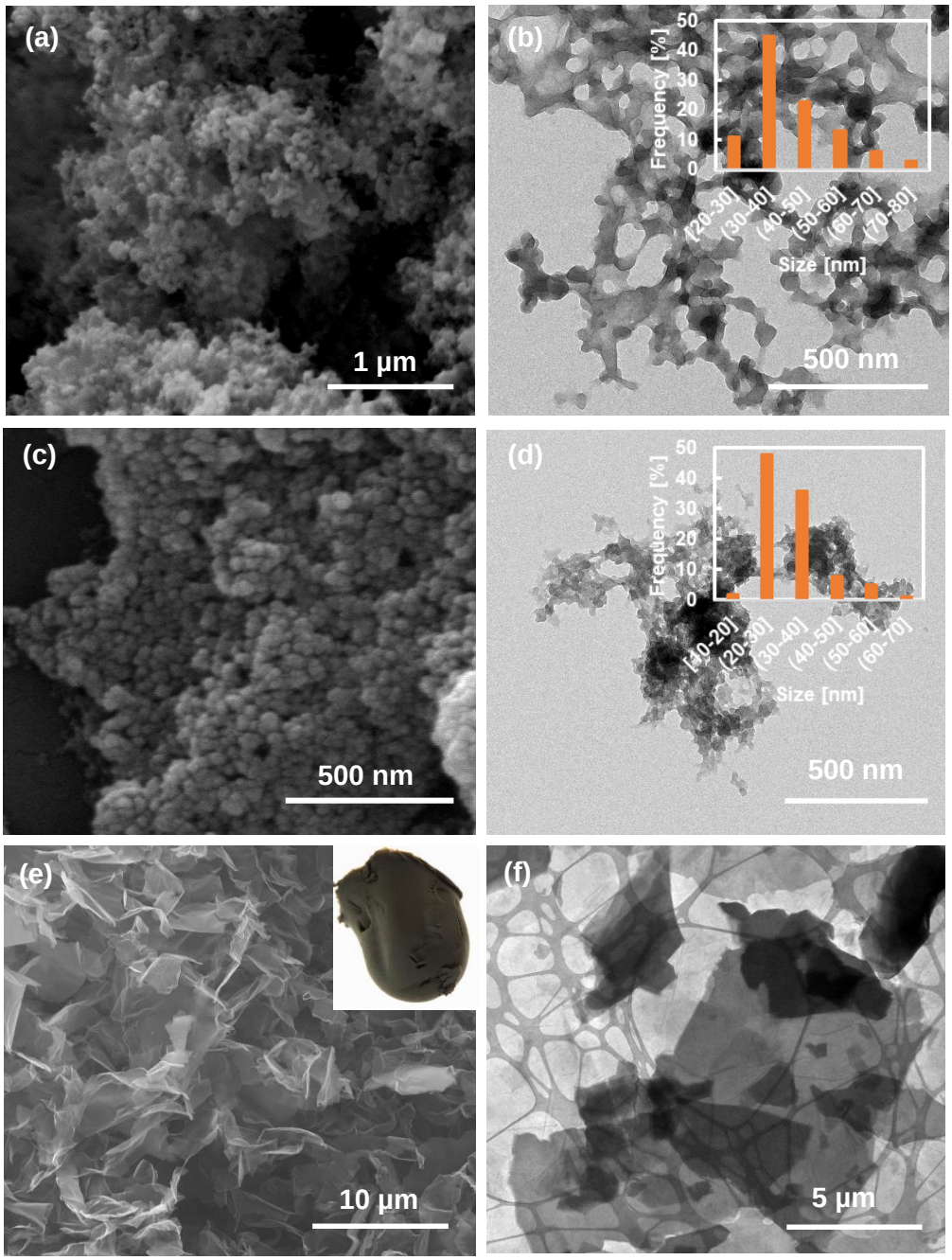

Figure 1. SEM (a,c,e) and TEM (b,d,f) pictures of individual composing materials: (a,b) *ex*_HK_{sc}, (c,d) *in*_HK_{sc}, and (e,f) cross section of the GO_{sc} aerogel and optical image of the cylindrical block in the inset of (e). TEM derived percentile size distribution histograms are shown for *ex*_HK_{sc} and *in*_HK_{sc} NPs in (b) and (d), respectively.

Table 2 shows the composing materials weight percentages determined for the different nanocomposite samples by ICP-MS, which closely matched the added initial weight ratios in the respective precursor dispersions (Table 1).

Table 2. Summary of the composition and textural properties, including BET surface area (Sa), apparent micropore surface area (μSa), BJH meso/macropore volume (mPv) and t-plot micropore volume (μPv), of the studied samples.

Sample	**GO:HKUST-1 ICP-MS [wt%]**	**Sa [m^2g^{-1}]**	**μSa [m^2g^{-1}]**	**mPv [cm^3g^{-1}]**	**μPv [cm^3g^{-1}]**
GO_{sc}	---	205	---	0.49	---
*ex*_HK_{sc}	---	1140	850	0.33	0.33
*in*_HK_{sc}	---	1210	945	0.89	0.37
*ex*_A_{sc}	54:46	760	555	0.29	0.22
*ex*_B_{sc}	36:64	1125	790	0.41	0.32
*ex*_C_{sc}	10:90	1520	1260	0.37	0.49
*in*_C_{sc}	14:86	1140	870	0.84	0.34

The XRD patterns recorded for the different HK@GO nanocomposites and the individual components are shown in the 2θ range 5-30º (Fig. S3). Pristine GO_{sc} exhibits a single wide peak at about 2θ=11°, compatible with highly oxidized graphene.[34] For pristine *ex*_HK_{sc} and *in*_HK_{sc} NPs, the patterns obtained were in accordance with the one simulated from the single crystal structure of HKUST-1.[35] The somehow low crystallinity observed for

*in*_HK_{sc}, with low-intensity XRD peaks (before normalization) and certain widening, reflects the small crystal size of the NPs. For the *in situ* samples, the XRD analysis was extended up to a 2θ of 50º to demonstrate that the precipitation of secondary phases, such as copper oxides (CuO or Cu_2O), was avoided using the designed protocol (Fig. S4). Both *ex situ* and *in situ* composites displayed the typical signals of the simulated HKUST-1. The rather broad peak of GO_{sc} at *ca.* 11º was not observed in any of the studied composite samples, not even in sample *ex*_A_{sc} with the highest GO percentage. This was probably due to a decrease in the staking of the GO nanoflakes caused by NPs interlayer deposition, rather than to the reduction of GO to rGO. Consistently with this reasoning, the typical rGO peak at 2θ *ca.* 25°[36] was not observed in any of the samples. To further elucidate the presence of GO *vs*. rGO in the aerogels, the sample *ex*_B_{sc}, with a significant percentage of GO, was analyzed by TGA and compared with composing materials GO_{sc} and *ex*_HK_{sc} (mass loss description can be found in the SI, Fig. S5). For the nanocomposite, a decay of weight in the interval 448-523 K was observed and attributed to the presence of oxygenated groups (hydroxyl and epoxy) in the GO component. This observation further supports the fact that the oxygenated groups in GO remain after $scCO_2$ processing, as it was already demonstrated for bare GO_{sc}.[19] The ATR-FTIR spectra measured in the region 4000-600 cm^{-1} for the different samples showed, exclusively, the typical vibration bands of HKUST-1 (for band assignation refer to the SI, Fig. S6).

Aerogel 3D nanostructures, with the shape of the used round bottom vials, were recovered for all the nanocomposites, with a bluish color provided by the HKUST-1 (Fig. 2insets). SEM pictures of aerogels cross-section revealed that the sponge-like skeleton observed for pristine GO_{sc} aerogel (Fig. 1e) remained unaltered in both types of prepared, *ex situ* and *in situ*, composites, which is exemplified in Fig. 2a,b with images of *ex*_C_{sc} and *in*_C_{sc}

samples. Some differences could be noticed in the distribution of the NPs throughout these aerogels. Whereas the NPs were well-dispersed and mostly disaggregated in the *ex situ* sample, in *in*_C_{sc} a worse distribution and higher degree of aggregation was observed. To further confirm the homogeneity of the *ex*_C_{sc} sample, EDS analysis was performed in a backscattered SEM image to identify the C, O, and Cu elemental composition in a piece of the aerogel. The mapping of the image established the homogeneous distribution of the three components (Fig. S7).

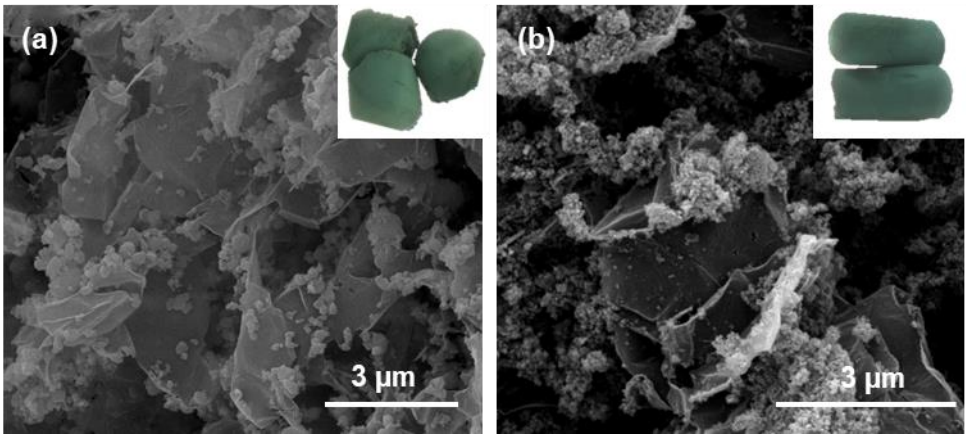

Figure 2. SEM images of aerogel composites: (a) *ex*_C_{sc} and (b) *in*_C_{sc}. The insets in the right up corners are optical pictures of the as-synthetized aerogel blocks.

3.2. N_2 adsorption/desorption measurements

3.2.1. Textural properties

The textural properties (Table 2) were determined by studying the specific physical adsorption and desorption of N_2 at low temperature (Fig. 3). Fig. 3a shows the isotherms of individual composing nanomaterials. GO_{sc} exhibits a type IV isotherm at low and medium p/p^0 and a type II isotherm at high p/p^0, which is characteristic of nanoporous structures with both meso and macropores. This isotherm has an H3-type hysteresis loop related to aggregates of plate-like particles.[37] The BET surface area measured for different samples of this material was in the order

of 200-210 m^2g^{-1}. The as-recovered *ex*_HK_{sc} nanopowder displayed a type I isotherm characteristic of microporous materials with a hysteresis loop at high relative pressures caused by the interparticle voids generated by NPs aggregation. A similar isotherm was observed for *in*_HK_{sc}, but with an increased uptake at nearly atmospheric pressure owing to the fluffy 3D structure obtained after the $scCO_2$ slow drying. However, these spongy products had a very fragile nature and break during manipulation. The apparent μSa was similar for both supercritically processed HKUST-1 samples (*ca.* 900 m^2g^{-1}), value that is slightly lower than the *ca.* 1300 m^2g^{-1} found for HKUST-1 activated NPs. This decrease in surface area is related to a decrease in the MOF crystallinity for different reasons. On one side, the presence of traces of water in the supercritical reactor during $scCO_2$ treatment would partially hydrolyze the HK NPs. In bare HKUST-1 samples, water can be strongly sorbed in the HKUST-1 micropores, dissolved in the CO_2 gas, as humidity, and so on. In the composites, water also appears as a residue from the H_2O/MeOH interchange process of GO and can be strongly sorbed on the GO surface. The impossibility of totally eliminating water from $scCO_2$ processing is a common issue of this technology,[38] which is particularly relevant in the studied system because of the nanometric size and the high sensitivity of HKUST-1 to water. It should be noted that water becomes extremely acidic in contact with $scCO_2$, which would speed the hydrolysis of the MOF. As reported for MOF-5, acid media could lead to the protonation of the ligands in the MOF resulting in the breakage of the Cu-O bond and leading to partial pore collapse.[39] On the other hand, the high pressure conditions inside the reactor could be a plausible reason for HKUST-1 irreversible amorphization due to compressive stress, originated during pore filling (pressurization) and pore emptying (depressurization), as previously described in $scCO_2$ for MOF-177.[40] Even a reduced amount of structural defects can cause a significant reduction in N_2 uptake due to pore blocking in the NPs outer surface.

N_2 isotherms for the *ex situ* nanocomposites are shown in Fig. 3b. The three samples exhibited high uptake at low relative pressures (type I), provided by the microporous nature of HKUST-1, and a continuous uptake with hysteresis loop at high pressures, denoting mesoporosity, originated by the 3D GO matrix. The values of the specific volume of adsorbed N_2 at the low p/p^0 increased proportionally to the amount of HKUST-1 in the composite, *i.e.*, *ex*_A_{sc} < *ex*_B_{sc} < *ex*_C_{sc}. Similarly, the values of apparent μSa and μPv increased with the percentage of HKUST-1 (Table 2). Sample *in*_C_{sc} also displayed a type I isotherm at low p/p^0 but with an increased adsorption at high p/p^0 (Fig. 3c), resembling *in*_HK_{sc}, which may be caused by the high degree of NPs aggregation, as formerly observed in Fig. 2b.

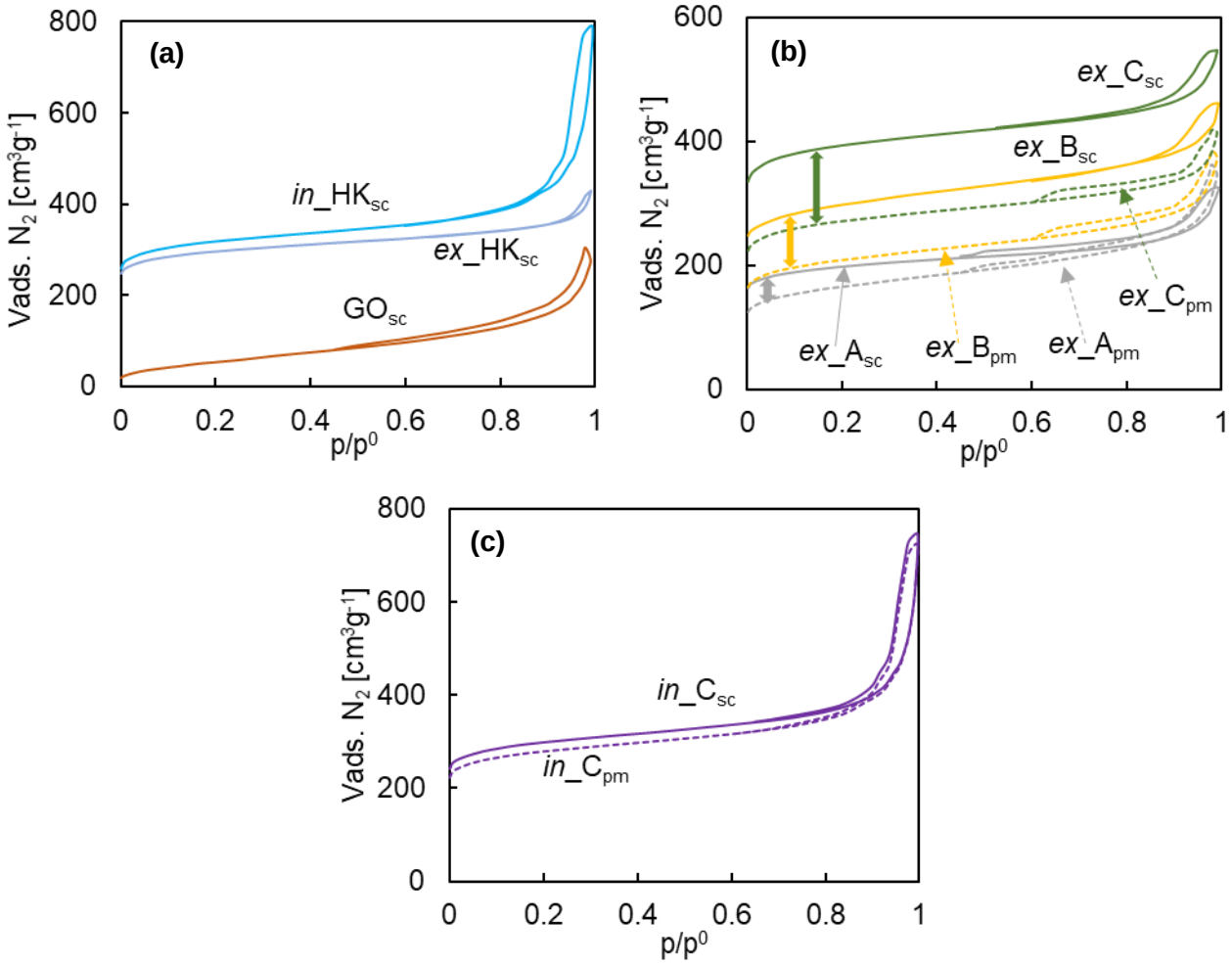

Figure 3. Low temperature N_2 adsorption/desorption experimental isotherms of: (a) net components, (b) *ex situ* and (c) *in situ* aerogel composites, experimental (straight lines) and calculated for physical mixtures (dotted lines).

To further analyze the textural properties of the nanocomposites, the measured N_2 adsorption isotherms and derived textural parameters were compared with the calculated quantities assuming a physical mixture (labeled as "pm"), obtained by integrating the respective weight percentage of each nanocomponent processed separately in $scCO_2$ (compounds GO_{sc} and *ex*_HK_{sc} or *in*_HK_{sc}). The calculated values are given in Table_S1, in comparison with the experimental ones. Results are graphically presented for *ex situ* and *in situ* samples in Fig. 3b,c, the analysis of which

indicated that the values of N_2 adsorption were consistently higher for the synthesized nanocomposites in comparison to the values estimated for the physical mixtures of equal composition, particularly for *ex situ* nanocomposites in which, quantitatively, this increase results in an enhancement of Sa values of 20, 40 and 45 % for samples *ex*_A_{sc}, *ex*_B_{sc} and *ex*_C_{sc}, respectively. This finding is considered a remarkable achievement and a clear indication of synergistic effects occurring between the nanomaterials in the nanocomposite. Synergistic effects improving gas adsorption have already been reported for the GO@HKUST-1 system, obtained by the *in situ* growth of HKUST-1 microcrystals with embedded GO nanosheets.[12,13] In these compounds, new micropores are described to be generated at the interface between both components. The same behavior can be extended to the *ex situ* HKUST-1@GO systems prepared in this work. However, in the studied nanoproducts, the differences between the micropore apparent surface area and volume of the composites and the correspondent physical mixtures are considered too high to be attributed only to this fact. A second reasonable possibility is to consider that the presence of GO prevents NPs from strong aggregation when following the *ex situ* approach, thus, reducing HKUST-1 micropore blocking. This would explain the higher microtextural values obtained for *ex*_C_{sc} with respect to *in*_C_{sc}, both with similar percentages of HKUST-1 but with the NPs displaying a different configuration, e.g., degree of aggregation, and distribution throughout the aerogel, as previously observed in SEM images (Fig. 2a,b).

3.2.2. Hierarchical pore size distribution

A hierarchical pore structure can be assigned to the studied composites involving multi-scale nanopores, reflected in a significant pore volume in both the micro and mesopore ranges, as can be straightforwardly deduced from the shape of the isotherms in Fig. 3b,c. Moreover, SEM micrographs indicate the presence of macropores in the composites (Fig. 2). To further illustrate

the hierarchical porous character of the synthetized products, DA and BJH plots of net GO_{sc} aerogel and *ex*_HK_{sc} NPs as well as composite *ex*_C_{sc} are shown in Fig. S8. Note that two different equations are necessary to describe pore filling in micropores (DA) and capillary condensation in mesopores (BJH). GO_{sc} aerogel displayed an almost null pore volume in the micropore region, while it has a wide pore size distribution in the whole mesopore scale. Contrarily, *ex*_HK_{sc} NPs have its pore volume predominantly distributed in the micropore region, while only a small percentage of it is situated in the mesopore region that is due to interparticle void. For the *ex situ* composite, substantial N_2 adsorption was observed at low p/p^0, indicating the predominant microporous character of the samples as shown by the DA plot. Moreover, a similar distribution to GO_{sc} mesopores can be observed in the BJH of the composite, indicating mesoporosity provided by the 3D nanostructuration of GO.

3.2.3. Kinetics of adsorption measured through equilibrium time

N_2 gas was used to analyze the kinetics of adsorption at different equilibrium times (10 and 120 s) by comparing the behavior of samples *ex*_C_{sc} and *ex*_C_{ad}, both similar in composition since they were synthetized from the same precursor dispersion (Table 1), only that the first one was obtained under $scCO_2$ and the second was air dried (see SI for *ex*_C_{ad} sample characterization). The air dried sample was obtained as a film at the bottom of the vial, and its dense morphology was established by SEM and XRD (Fig. S9a,b,c). N_2 adsorption analysis showed the absence of mesoporosity in the dense air dried product (Fig. S9d, Table S2). The increase of the equilibrium time, from 10 (routine) to 120 s, produced different effects in the two samples (Fig. S9d). On one hand, two superimposed isotherms were obtained by measuring the aerogel *ex*_C_{sc} at both equilibrium intervals. Conversely, a noteworthy increase on the N_2 adsorption values (*ca.* 35 v%) of the isotherm recorded for *ex*_C_{ad} was observed by delaying 120 s the measurement between two

equilibrium points, which results in a significant increase of measured micropore apparent surface area and volume (Table S2). This set of experiments was performed to illustrate that the loss of the hierarchical nanoporous architecture in the *ex*_C_{ad} sample negatively affects the adsorption kinetics, since the air dried sample needed extra time to reach equilibrium.[41] Hence, it can be concluded that the hierarchical combination in an aerogel composite of a mesoporous matrix and microporous NPs is beneficial, since micropores would provide for a high adsorption capacity, while mesopores enhance gas diffusion and kinetics, favoring an easy access to the micropores in the HKUST-1, which is not possible following a conventional evaporation method.

3.2.4. Chemical sensibility to water

Water vapor, including atmospheric humidity, has a destructive effect on the structure of HKUST-1, being more detrimental for nanometric particles with significant external surface for hydrolysis.[42] The role of essentially hydrophobic rGO as a potential protective agent in a humid atmosphere has been reported in the literature for HKUST-1/graphene composites.[43,44] This analysis was extended here to the materials prepared in this work, containing highly oxygenated GO with a primary hydrophilic character. N_2 adsorption was used to evaluate the chemical sensibility to water of a selected composite (*ex*_C_{sc}) *vs.* *ex*_HK_{sc} NPs. Variations on N_2 adsorption were measured for the sample just as-recovered from the high pressure reactor and after a period of three weeks under 60-75 % relative humidity (Fig. S10). A similar reduction of *ca.* 25 v% in the values of N_2 adsorption was observed for both pristine NPs and nanocomposite material. This behavior is related in both cases to HKUST-1 NPs degradation by water. Nevertheless, this result also demonstrated that the presence of hydroxyl and epoxy functionalities in GO did not accelerate the process of HKUST-1 NPs degradation due to hydrolysis.

3.2.5. Mechanical stability

The macrostructural mechanical stability of the aerogels was confirmed in regard of static adsorption by performing cycles of N_2 adsorption/desorption in sample *ex*_C_{sc}. Obtained isotherms are shown in Fig. S11a, demonstrating the complete stability of the sample in regard of adsorption and no affectation towards kinetics, as the duration of the adsorption/desorption process was maintained in the five studied cycles (Fig. S11b). After five cycles, the recovered sample showed similar cylindrical visual appearance, structure determined by XRD (Fig. S11c) and morphological aspect observed by SEM (Fig. S11d) than the original sample (Fig. 2a).

3.2.6. Volumetric working capacity

Aside from enhanced absolute uptakes and gravimetric working capacity (moles of gas adsorbed per unit mass of adsorbent) and good mass transfer kinetics, even flow distribution and no fluidization, highly nanoporous structured adsorbents should also exhibit a satisfactory volumetric working capacity (loading per unit system volume), commonly associated with compensating low voidage for minimizing the size of the adsorbent. In general, aerogels are materials with low values of bulk density, and the supercritically prepared GO aerogels in this work are not an exception. Certainly, a density value in the order of only 5 $mgcm^{-3}$ was calculated for the as-synthesized GO_{sc} aerogel. Density values increased to *ca.* 7, 14, and 32 $mgcm^{-3}$ for *ex*_A_{sc}, *ex*_$B_{sc,}$ and *ex*_C_{sc} composites, respectively. Hence, the large percentages of empty void space in aerogels could compromise their volumetric adsorption capacity. This characteristic can be considered a drawback especially important in industrial applications in which the adsorbent must be confined in a given volume. The disadvantage of low volumetric adsorption in aerogels could be solved by applying mechanical densification to the prepared aerogel cylinders, attaining a compromise between enhancing the volumetric working capacity and maintaining fast gas

diffusion kinetics. To proof this aspect in this work, mechanical densification of the aerogels was manually carried out by using a 2 mL syringe, sealed at the end with Teflon, and filled with aerogel cylinders of GOsc and *ex*_C_{sc} samples (Fig. 4a). By using this device, an increase in the bulk density of 30 and 5-fold, respectively, was easily attained. Consequently, the resulting values of density for compressed *ex situ* composites were above 150 $mgcm^{-3}$, closer to that of pristine HKUST-1 NPs, measured in this work as 280 $mgcm^{-3}$. Importantly, the microporous and mesoporous characteristics were preserved in the N_2 isotherms of the compressed aerogels (Fig. 4b). For these nanocomposites, even if mechanical pressing caused the visual collapse of the aerogel macrostructure due to the destruction of large macropores, the SEM analysis indicates that the nanoporous internal framework originated by GO flakes assembly was, at least, partially preserved, as shown in Fig. 4c,d for densified GO_{sc} (ρx30) and *ex*_C_{sc} (ρx5) samples.

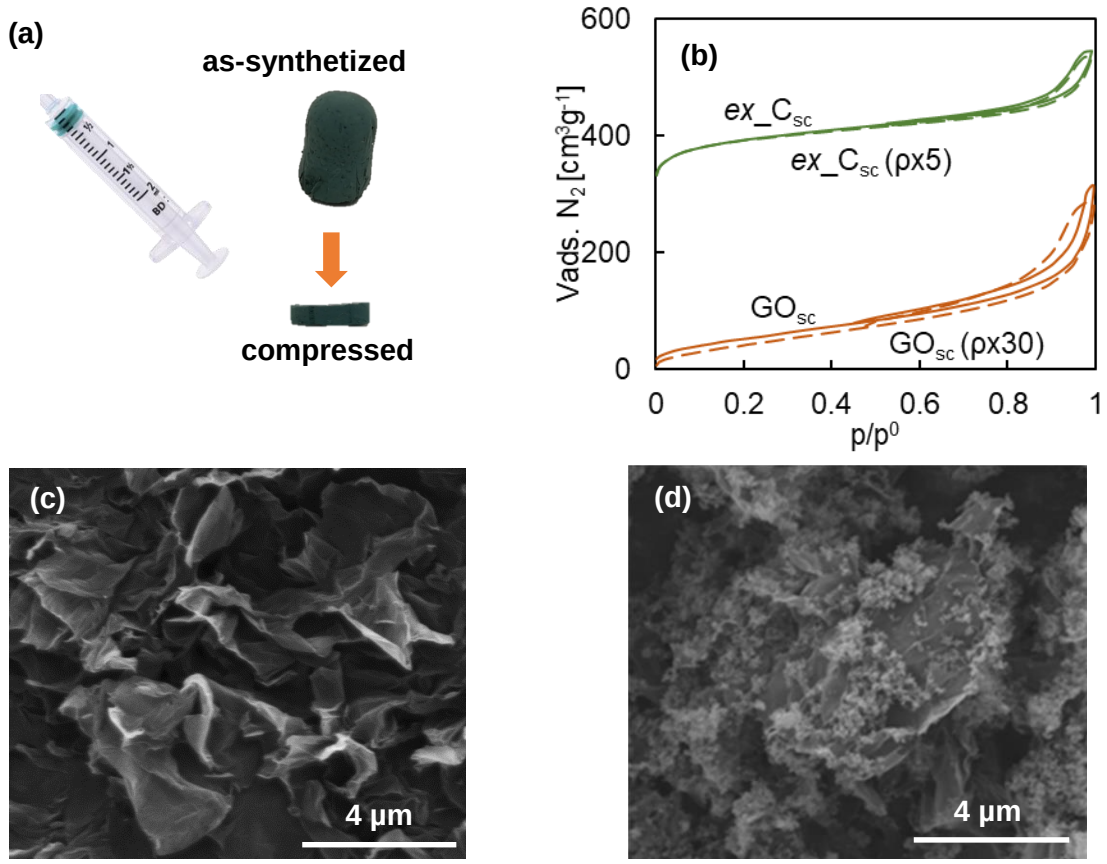

Figure 4. Characterization of the mechanically compressed samples GO_{sc} (ρx30) and *ex*_C_{sc} (ρx5): (a) device used for mechanical densification an optical pictures of the *ex*_C_{sc} composite as-synthetized and compressed, (b) N_2 isotherms, and SEM pictures of compressed GO_{sc} (c) and *ex*_C_{sc} (d).

3.3. CO_2 adsorption measurements

Enhanced adsorption capacity for polarizable gasses, such as CO_2, at low pressures is commonly observed for MOFs in which the removal of terminal bound solvent molecules exposes coordinative unsaturated metal centers, as it is the case of HKUST-1.[45] For example, the measured CO_2 uptakes in the *ex*_HK_{sc} sample at atmospheric pressure and 273 K was relatively high, of the order of 6.6 $mmolg^{-1}$, in comparison to bare GO_{sc}, with adsorption values of only 1.1 $mmolg^{-1}$ (Fig.

5a). The studied nanocomposites *ex*_C_{sc} and *in*_C_{sc} samples provided similar values to bare HKUST-1, around 6.0 and 5.5 mmol g^{-1}, respectively (Fig. 5b).

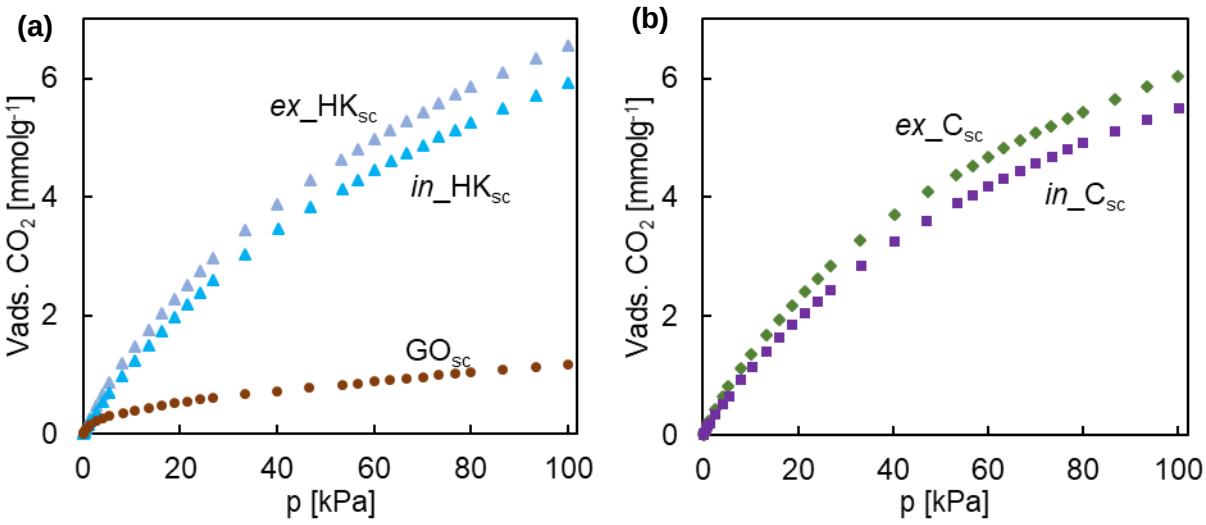

Figure 5. CO_2 adsorption isotherms at 273 K for representative studied products: (a) scCO_2 treated HKUST-1 and GO, and (b) selected nanocomposites.

To understand the behavior of nanoporous materials in applications such as gas separation, information about the temperature dependency of the adsorption isotherms becomes necessary. This information can be summarized in the isosteric heat of adsorption, used to describe the average enthalpy of adsorption of the gas at a specific surface coverage. This variable is directly related to the interaction between adsorbate molecules and the surface of the adsorbent. In this work, Q_{st} was evaluated by collecting CO_2 adsorption isotherms up to 0.1 MPa at 273, 298 and 313 K for each pristine component, GO_{sc} (Fig. S12a) and NPs of activated HK at 433 K, *ex*_HK_{sc} and *in*_HK_{sc} (Fig. S12b), and composites *ex*_C_{sc} (Fig. S12c) and *in*_C_{sc} (Fig. S12d). For all the studied compounds, the amount of adsorbed CO_2 decreases with the increase of temperature, indicating exothermic sorption. Calculated Q_{st} values at different surface coverages are shown in Fig. S13. For activated HK NPs, a constant Q_{st} value of -24 $Jmmol^{-1}$ was obtained, independent of

the fractional coverage, indicating an energetically homogeneous adsorbent surface. This value is in agreement with the computational enthalpy of adsorption calculated for the pair CO_2/HKUST-1.[46] The supercritically treated *ex*_HK_{sc} and *in*_HK_{sc} samples also displayed a nearly constant Q_{st} value of -25 $Jmmol^{-1}$ up to a surface coverage of 2 $mmolg^{-1}$ of CO_2. In the case of GO_{sc}, a clear decrease of $-Q_{st}$ from 30 to 16 $Jmmol^{-1}$ was noticed when increasing surface coverage, denoting heterogeneity of GO energy surface, caused by the presence of a great range of functionalities and possible defects. Due to the low percentage of GO in the studied composites (*ca.* 10 wt%), these products have similar behavior to HK NPs composing units, maintaining the CO_2 affinity nearly constant with Q_{st} values of *ca.* -25 $Jmmol^{-1}$. The high CO_2 uptake and low and constant Q_{st} make nanocomposite aerogels promising materials for CO_2 gas separation.[47]

3.4. High-pressure CH_4 adsorption

Natural gas, mainly composed of methane, is considered a more sustainable transportation fuel in comparison to other traditional fossil fuels, principally due to its abundant natural reserves, reduced pollutant (CO_2) emissions, and high hydrogen to carbon ratio.[48] However, the use of this fuel in vehicles has, currently, a critical bottleneck related to its low storage density at ambient temperature. A key challenge is to find a nanoporous material being mass- and volume-efficient, with ambient-temperature high-density storage capacity *via* physisorption.[49] In this respect, HKUST-1 has been reported to be sizable for methane adsorption (CH_4 molecular kinetic diameter = 0.38 nm), since this MOF contains three types of cages with pore diameters of *ca.* 0.5, 1.1 and 1.3 nm.[50] Dense CH_4 adsorption at 298 K and up to 10 MPa was analyzed in this work for the *ex*_C_{sc} nanocomposite, as well as for bare GO_{sc} aerogel and *ex*_HK NPs composing units. Important parameters considered in assessing the material performance for CH_4 uptake were the volumetric and gravimetric working capacities.

Total CH_4 gravimetric adsorption [$g_{CH4}g_{adsorbent}^{-1}$] capacities of the different studied samples at 298 K are plotted as a function of pressure in Fig. 6a. Pristine GO_{sc} displayed a type III isotherm, denoting physisorption with low energetic interactions between CH_4 and the adsorbent, while the isotherm of bare *ex*_HK_{sc} NPs resembled type I, with significant uptake at low pressures and tendency to reach a plateau, typical of a microporous compound. The nanocomposite *ex*_C_{sc} displayed a Type II isotherm, with increased uptake at low pressures and deprived of adsorption restrictions at high pressures. Samples *ex*_C_{sc} and *ex*_HK_{sc} had a similar gravimetric uptake at low pressures, provided by the MOF microporosity, but at pressures higher than 0.5 MPa, the contribution of the meso/macroporous nature of the GO matrix became important and, as a result, a significant adsorption was observed for the nanocomposite up to a pressure of 10 MPa. The total uptake at 10 MPa was 0.28 gg^{-1}, a value considerably higher than others reported in the literature for pristine HKUST-1 with gravimetric uptake values around 0.18 gg^{-1}.[51] The deliverable gravimetric capacity under practical working conditions is estimated as the difference in the uptake at the industrially viable maximum (*e.g.*, 10 MPa) and minimum (*e.g.*, 0.5 MPa) working pressures.[52] Hence, type I isotherm, always obtained for bare microporous HKUST-1, would lead to a low gravimetric working capacity due to high uptake at low pressures followed by a plateau. Increased gravimetric working capacities are obtained for adsorbents with the sigmoid isotherm type II, here observed for the studied nanocomposite *ex*_C_{sc} aerogel, which exhibits more than 2-fold the working capacity of net *ex*_HK_{sc} NPs. This is a remarkable result that highlights the importance of the hierarchical nanoporous structure on the composites for industrial high pressure applications.

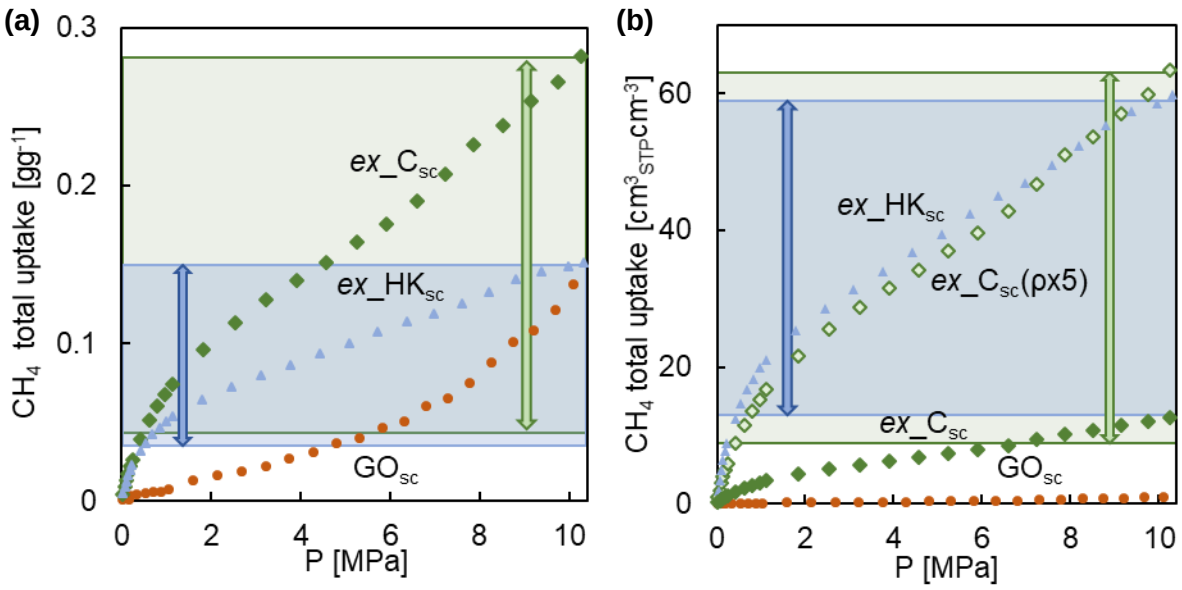

Figure 6. CH_4 adsorption isotherms up to 10 MPa at 298 K representing: (a) gravimetric, and (b) volumetric uptakes. Blue and green square shows the practical working capacity of *ex*_HK_{sc} and *ex*_C_{sc}, respectively.

The absolute volumetric uptake [$cm_{CH4STP}^3 cm_{adsorbent}^{-3}$] was calculated for these samples from the gravimetric adsorption isotherms by using the density values of the adsorbent and that of CH_4 at STP under working conditions (0.0007 gcm^{-3}). Calculated values are plotted in Fig. 6b. The calculated volumetric adsorption values for *ex*_HK_{sc} at different pressures were, to a certain extent, lower than reported for other pristine HKUST-1 systems,[51,53] which is partially ascribed to the somewhat lower micropore volume values in NPs *vs.* commonly used microparticles, and also to the lower density value used for the calculation. In the literature the density value of either the non-activated sample (*ca.* 400 $mgcm^{-3}$) or even the crystallographic value (883 $mgcm^{-3}$) is frequently employed.[53] However, in this study, it has been considered more realistic to use the density value measured for the activated NPs (280 $mgcm^{-3}$). As expected, the values of volumetric adsorption for the as-recovered aerogels were very small in the range of studied pressures (Fig. 6b), but the drawback of low volumetric adsorption can be easily solved by sample densification,

as previously explained. Indeed, the mechanical compression of the *ex*_C_{sc} (ρx5) nanocomposite up to a density of 160 mgcm^{-3}, would drastically improve the CH_4 uptake on a volumetric basis, without losing sample permeability as formerly demonstrated for N_2 adsorption (Fig. 4b), even achieving higher volumetric working capacities than net *ex*_HK_{sc} sample (Fig. 6b). On the contrary, densification of strictly microporous materials often results in pore blocking and comes at the expense of slow adsorption kinetics.[51]

3.5. Dynamic adsorption measurements

Dynamic gas sorption in fixed-bed columns is a commonly used standard test to evaluate the gas separation capability of a specific adsorbent.[54] The conventional procedure to prepare fixed-bed columns for gas separation consists in packing adsorbent powder together with an inert material needed for flow distribution. Important drawbacks of this method are the high amount of adsorbent required and the lack of consistency in adsorbate diffusion. Currently, industrial efficient dynamic gas separation processes are preferentially performed by nanostructuring the solid into monoliths, foams, pellets or extrudes of aggregated crystals.[55] The use of nanostructured 3D adsorbents in semi-continuous processes performed under flow commonly decreases the vulnerability to compaction and consequent pressure drop compared to packed bed systems.[56] For instance, structured MOF adsorbents have been obtained by applying high pressure to microcrystalline powders, involving occasionally polymeric binders.[57,58] However, crystals sintering and compression stress on micropores have been described to have detrimental effects regarding total gas uptake and kinetics.[51] In view of that, composites involving MOF particles have been deeply explored to improve sorption characteristics.[10] In this work, HKUST-1@GO aerogels have been considered as good candidates to act as the stationary phase in dynamic gas separation processes due to the hierarchical nanopore structure of the material. For this

application, N_2/CO_2 and CH_4/CO_2 separations were explored. The former is relevant in post-combustion CO_2 capture,[59] while the latter is important in applications of natural gas upgrading.[60] These three gases are characterized by a zero dipole moment and a comparable kinetic diameter (3.3, 3.6, and 3.8 Å for CO_2, N_2, and CH_4, respectively), which make challenging their separation due to the close similarity between molecules. The main appreciable difference in terms of physical properties is the significant quadrupole moment shown by CO_2, which is minimum for N_2 and negligible for CH_4.[61] This difference leads to lower HKUST-1 -Q_{st} values for N_2 and CH_4, reported as 15.5 and 17 $Jmmol^{-1}$, respectively,[46,50] than for CO_2, measured as 25 $Jmmol^{-1}$ in this work. In this respect, the charge-dense points of HKUST-1, with open metal sites, provide an opportunity for discriminating CO_2 in gas mixtures based on its quadrupole moment.[45] Gas uptakes at 273 K and atmospheric pressure were first measured in sample *ex*_C_{sc} to have an indication of nanocomposite affinity for the different gases. Obtained loadings were 0.2, 1.3 and 6.0 $mmolg^{-1}$ for N_2, CH_4 and CO_2, respectively. Hence, the synthetized nanocomposites are expected to display a significant selectivity for CO_2 adsorption when mixtures of these gases are used, since measured CO_2 uptake was *ca.* 5 and 30 fold higher when compared with CH_4 and N_2, respectively.

An additional advantage of the used supercritical CO_2 methodology is the fact that it permits the straightforward fabrication of the aerogels inside a fixed-bed column. For gas separation analysis, aerogels, either of bare GO_{sc} or composed with HKUST-1 NPs, were grown inside stainless steel columns, following the described *ex situ* or *in situ* $scCO_2$ protocol, which were further inserted in a gas chromatograph system (Fig. S2). The aerogels were formed with the shape of the columns (cylinders), filling most of the empty space (Fig. 7, middle). The columns were used to evaluate the separation performance of the aerogels by performing dynamic breakthrough experiments of binary N_2/CO_2 and CH_4/CO_2 mixtures at 273 K in a volumetric ratio of 85:15 v/v%.

The mass of the aerogels grown inside the columns was weighted as 15 and 100 mg for pristine GO_{sc} and *ex*_C_{sc} or *in*_C_{sc} samples, respectively. Using these mass values, the breakthrough time was normalized to 1 g in the plots of Fig. 7. For the pristine aerogel GO_{sc}, the outlet gas concentration rapidly matches the feed gas concentration, being the CO_2 breakthrough time of only a few seconds for both studied gas mixtures (Fig. 7a,b), thus indicating the very low capacity of this nanomaterial for the separation of the studied gasses. Contrarily, for the examined nanocomposites, the CO_2 breakthrough time was of *ca.* 20 $ming^{-1}$ for both N_2/CO_2 (Fig. 7c,e) and CH_4/CO_2 mixtures (Fig. 7d,f). As expected, CO_2 was selectively adsorbed in the composites, giving rise to a large elapsed time for these adsorbents. In order to quantify the CO_2 selectivity, it was first required to calculate the total uptake of each gas (q_i), as explained in section 2.3.2. The calculated q for CO_2 was *ca.* 1.4 $mmolg^{-1}$ in the composites, value close to the one observed in CO_2 isotherms of both studied samples (Fig. 5b) at p_{CO2} = 15 kPa, which is the corresponding partial pressure of CO_2 in the process. This value was *ca.* 1.7 $mmolg^{-1}$ for CH_4 and close to zero for N_2 at their working pressure (p = 85 kPa). Hence, the selectivity of CO_2 over N_2 could not be accurately calculated, though it could be graphically confirmed in the separation curves shown in Fig. 7c,e. For the CO_2/CH_4 mixture, the selectivity was calculated as 4.7, value similar to the one estimated from the gas uptakes at 273 K and 0.1 MPa, *i.e.*, *ca.* 5.0.

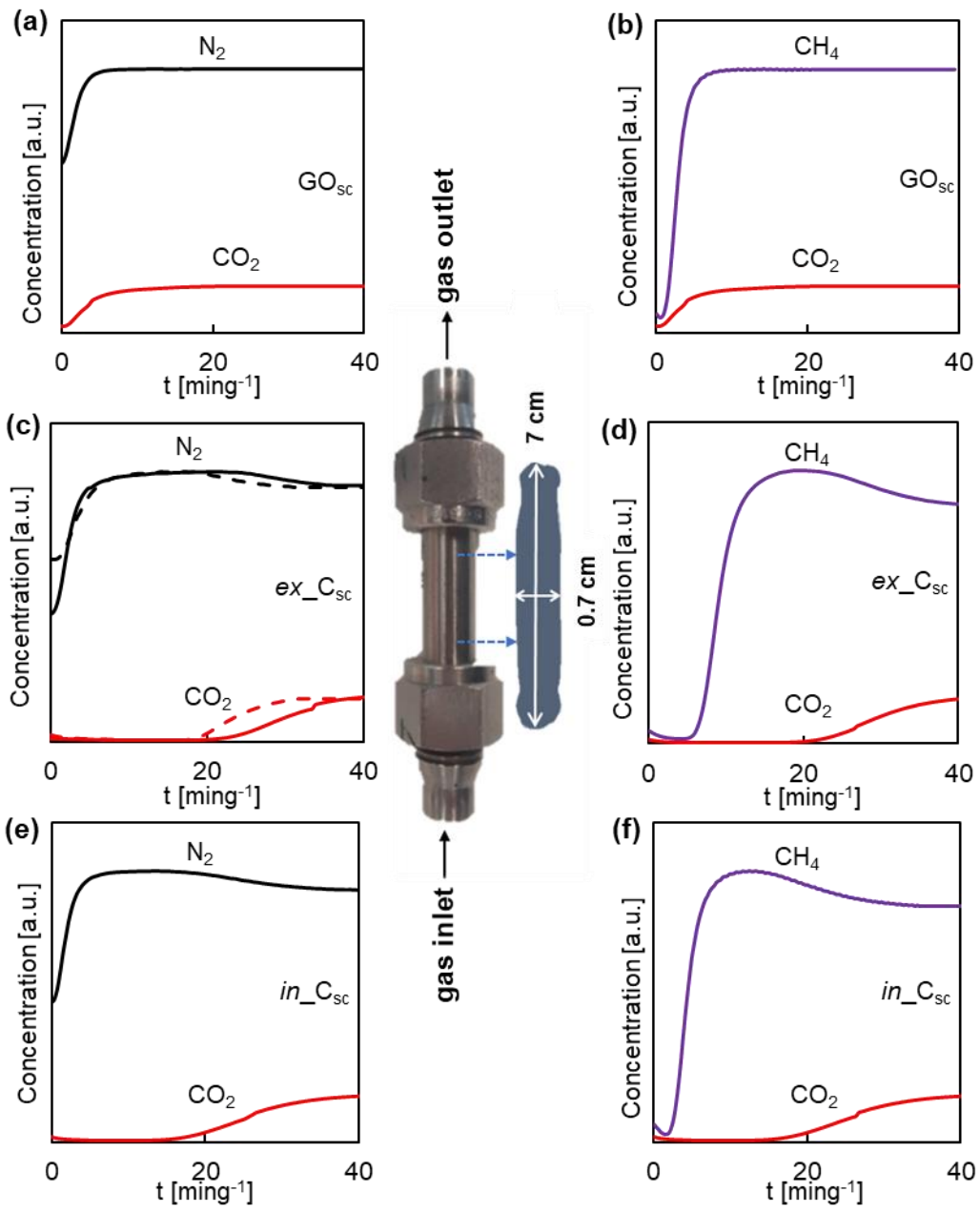

Figure 7. 1st cycle breakthrough curves obtained at 273 K and 0.1 MPa for gas mixtures of N_2/CO_2 and CH_4/CO_2, both at 85:15 v/v% and 10 $mLmin^{-1}$ flow: (a,b) GO_{sc}, (c,d) *ex*_C_{sc}, and (e,f) *in*_C_{sc} (dashed lines in (e) correspond to the 5th cycle). Arbitrary units are used in axis *y* because the system also detects He. The used column and the extracted *ex*_C_{sc} aerogel grown inside is shown in the middle.

The presented design of the chromatographic columns (Fig. S2) has several benefits. First, the nanocomposite hierarchical nanoporosity, involving micro and meso/macropores provided by the MOF and GO nanocomponents, together with the low-packing density and good distribution of the adsorptive moieties along the axial direction of the column, would facilitate gas diffusion, allowing to easily reach thermodynamic equilibrium of adsorption in all the MOF NPs. Second, as it has been described for foam adsorbents, the flow friction and hence the pressure drop is expected to decrease in aerogels due to the presence of wide channels in a network of interconnected voids, which allow the radial mixing of the flow.[62] Potential fluidization or severe flow resistance in column operation are prevented by immobilizing the nanoparticulate adsorbent on GO supporting material. Finally, nanostructuring the composites in the form of aerogel cylinders avoids the collapse of the structure at high flow due to mechanical forces and increases the reusability of the adsorbent in prolonged cyclic operation, which is an important technical parameter in industrial gas separation processes.[63] To test this parameter, multi-cycle tests (up to five) of N_2/CO_2 separation were performed for sample *ex*_C_{sc} (see doted lines in Fig. 7e). This result indicates that the column exhibits satisfactory performance over long-term operation.

4. Conclusions

Ex situ and *in situ* supercritical CO_2 methods were used for the preparation of GO-based nanocomposite 3D nanostructures, avoiding its reduction to rGO and allowing the control of nanocomponents fraction. The composite HKUST-1@GO was chosen in this work as the case study to exemplify the potential advantages of the method on the preparation of gas adsorbents. The obtained aerogel nanocomposites display hierarchical nanoporosity with a mixture of micro and meso/macroporosity that is maintained even after performing

mechanical compression. It is proved that the presence of GO in the nanocomposite does not compromise the chemical stability of the MOF nanoparticles, but rather fosters adsorption by synergistic effects. The generation of new micropores at the interface between the composite nanocomponents, and the increase of accessible MOF micropores, originated by the decrease of NPs aggregation are two potential reasons for the observed synergy. Similar to HKUST-1, CO_2 adsorption Q_{st} values for aerogel nanocomposites remain low and nearly constant during the whole range of studied surface coverage, which is commonly demanded in applications related to gas separation. Nanocomposites were used to investigate their separation performance for N_2/CO_2 and CH_4/CO_2 gas mixtures in dynamic flow experiments, showing that breakthrough times for CO_2 of nearly 20 min g^{-1} could be reached and maintained for several cycles. Remarkably, regarding high pressure CH_4 adsorption, the studied nanocomposite exhibited more than 2-fold the gravimetric working capacity of pristine HKUST-1 nanoparticles, holding a sigmoid isotherm (type II), commonly desired in high pressure processes. The newly developed methodology to obtain aerogels from drying alcogels with $scCO_2$ has clear advantages *versus* the conventional air drying protocols, where powders are obtained, in regard of gas adsorption and kinetics, since, on one hand, it makes possible to maintain GO exfoliated generating meso/macroporosity and, on the other hand, the use of gels as precursors allows the shaping of the final product. The developed method can be applied to a large number of solid nanocomposites in which having a GO matrix is an advantage.

Supporting information

Schematic representation of the synthetic steps. Gas separation set-up. XRD graphs. TGA graphs and description. ATR-FTIR graphs and description. EDS images. Pore size distribution. Tabulated

textural properties. Tabulated textural properties and kinetics description of N_2 diffusion. Characterization of air dried samples. Humidity effect. Cyclic N_2 adsorption/desorption. CO_2 adsorption isotherms. Isosteric heats of adsorption.

Acknowledgements / Funding

This work was supported by the Spanish Ministry of Science and Innovation MICINN through the Severo Ochoa Program for Centers of Excellence (SEV-2015-0496 and CEX2019-000917-S) and the Spanish National Plan of Research with projects CTQ2017-83632, PID2020-115631GB-I00, CTQ2016-75150-R, CTQ2017-84692-R, RTI2018-100832-B-I00 and PID2019-106832RB-I00. J.A.R.N. thanks Junta de Andalucia (P18-RT-612). K.C.S. thanks the Department of Chemistry through start-up funding. This work has been done in the framework of the doctoral program "Chemistry" of the Universitat Autònoma de Barcelona by A.R., A.B. and J.F.; A.R. and A.B. acknowledge FPI grants.

References

(1) Seal, S.; Karn, B. Safety Aspects of Nanotechnology Based Activity. *Saf. Sci.* **2014**, *63*, 217–225. https://doi.org/10.1016/j.ssci.2013.11.018.

(2) Rezaei, F.; Webley, P. Structured Adsorbents in Gas Separation Processes. *Sep. Purif. Technol.* **2010**, *70* (3), 243–256. https://doi.org/10.1016/j.seppur.2009.10.004.

(3) Rezaei, F.; Mosca, A.; Webley, P.; Hedlund, J.; Xiao, P. Comparison of Traditional and Structured Adsorbents for Co2 Separation by Vacuum-Swing Adsorption. *Ind. Eng. Chem. Res.* **2010**, *49* (10), 4832–4841. https://doi.org/10.1021/ie9016545.

(4) Kemp, K. C.; Seema, H.; Saleh, M.; Le, N. H.; Mahesh, K.; Chandra, V.; Kim, K. S. Environmental Applications Using Graphene Composites: Water Remediation and Gas Adsorption. *Nanoscale* **2013**, *5* (8), 3149–3171. https://doi.org/10.1039/c3nr33708a.

(5) Gadipelli, S.; Guo, Z. X. Graphene-Based Materials: Synthesis and Gas Sorption, Storage and Separation. *Prog. Mater. Sci.* **2015**, *69*, 1–60. https://doi.org/10.1016/j.pmatsci.2014.10.004.

(6) Rezvani Jalal, N.; Madrakian, T.; Afkhami, A.; Ghoorchian, A. In Situ Growth of Metal-Organic Framework HKUST-1 on Graphene Oxide Nanoribbons with High Electrochemical Sensing Performance in Imatinib Determination. *ACS Appl. Mater. Interfaces* **2020**, *12* (4), 4859–4869.

https://doi.org/10.1021/acsami.9b18097.

(7) Martín-Jimeno, F. J.; Suárez-García, F.; Paredes, J. I.; Enterría, M.; Pereira, M. F. R.; Martins, J. I.; Figueiredo, J. L.; Martínez-Alonso, A.; Tascón, J. M. D. A "Nanopore Lithography" Strategy for Synthesizing Hierarchically Micro/Mesoporous Carbons from ZIF-8/Graphene Oxide Hybrids for Electrochemical Energy Storage. *ACS Appl. Mater. Interfaces* **2017**, *9* (51), 44740–44755. https://doi.org/10.1021/acsami.7b16567.

(8) Li, H.; Wang, K.; Sun, Y.; Lollar, C. T.; Li, J.; Zhou, H. C. Recent Advances in Gas Storage and Separation Using Metal–Organic Frameworks. *Mater. Today* **2018**, *21* (2), 108–121. https://doi.org/10.1016/j.mattod.2017.07.006.

(9) Kang, Z.; Fan, L.; Sun, D. Recent Advances and Challenges of Metal-Organic Framework Membranes for Gas Separation. *J. Mater. Chem. A* **2017**, *5* (21), 10073–10091. https://doi.org/10.1039/c7ta01142c.

(10) Ahmed, I.; Jhung, S. H. Composites of Metal-Organic Frameworks: Preparation and Application in Adsorption. *Mater. Today* **2014**, *17* (3), 136–146. https://doi.org/10.1016/j.mattod.2014.03.002.

(11) Petit, C.; Bandosz, T. J. MOF-Graphite Oxide Nanocomposites: Surface Characterization and Evaluation as Adsorbents of Ammonia. *J. Mater. Chem.* **2009**, *19* (36), 6521–6528. https://doi.org/10.1039/b908862h.

(12) Petit, C.; Burress, J.; Bandosz, T. J. The Synthesis and Characterization of Copper-Based Metal-Organic Framework/Graphite Oxide Composites. *Carbon N. Y.* **2011**, *49* (2), 563–572. https://doi.org/10.1016/j.carbon.2010.09.059.

(13) Bandosz, T. J.; Petit, C. MOF/Graphite Oxide Hybrid Materials: Exploring the New Concept of Adsorbents and Catalysts. *Adsorption* **2011**, *17* (1), 5–16. https://doi.org/10.1007/s10450-010-9267-5.

(14) Muschi, M.; Serre, C. Progress and Challenges of Graphene Oxide/Metal-Organic Composites. *Coord. Chem. Rev.* **2019**, *387*, 262–272. https://doi.org/10.1016/j.ccr.2019.02.017.

(15) Maskim Vladimirovich, G.; Pavlovich Melnikov, V. Graphene Oxide/Reduced Graphene Oxide Aerogels. *Graphene Oxide Appl. Oppor.* **2018**, 39–55. https://doi.org/10.5772/intechopen.73080.

(16) Zhang, X.; Liang, Q.; Han, Q.; Wan, W.; Ding, M. Metal-Organic Frameworks@graphene Hybrid Aerogels for Solid-Phase Extraction of Non-Steroidal Anti-Inflammatory Drugs and Selective Enrichment of Proteins. *Analyst* **2016**, *141* (13), 4219–4226. https://doi.org/10.1039/c6an00353b.

(17) Zhao, S.; Malfait, W. J.; Guerrero-Alburquerque, N.; Koebel, M. M.; Nyström, G. Biopolymer Aerogels and Foams: Chemistry, Properties, and Applications. *Angew. Chemie - Int. Ed.* **2018**, *57* (26), 7580–7608. https://doi.org/10.1002/anie.201709014.

(18) Gurikov, P.; Raman, S. P.; Weinrich, D.; Fricke, M.; Smirnova, I. A Novel Approach to Alginate Aerogels: Carbon Dioxide Induced Gelation. *RSC Adv.* **2015**, *5* (11), 7812–7818. https://doi.org/10.1039/c4ra14653k.

(19) Borrás, A.; Gonçalves, G.; Marbán, G.; Sandoval, S.; Pinto, S.; Marques, P. A. A. P.; Fraile, J.; Tobias, G.; López-Periago, A. M.; Domingo, C. Preparation and Characterization of Graphene Oxide Aerogels: Exploring the Limits of Supercritical CO2 Fabrication Methods. *Chem. - A Eur. J.* **2018**, *24* (59), 15903–15911. https://doi.org/10.1002/chem.201803368.

(20) Borrás, A.; Fraile, J.; Rosado, A.; Marbán, G.; Tobias, G.; López-Periago, A. M.; Domingo, C. Green and Solvent-Free Supercritical CO 2 -Assisted Production of Superparamagnetic Graphene

Oxide Aerogels: Application as a Superior Contrast Agent in MRI . *ACS Sustain. Chem. Eng.* **2020**, *8* (12), 4877–4888. https://doi.org/10.1021/acssuschemeng.0c00149.

(21) Czaja, A. U.; Trukhan, N.; Müller, U. Industrial Applications of Metal–Organic Frameworks. *Chem. Soc. Rev.* **2009**, *38* (5), 1284–1293. https://doi.org/10.1039/b804680h.

(22) Liu, X. W.; Sun, T. J.; Hu, J. L.; Wang, S. D. Composites of Metal-Organic Frameworks and Carbon-Based Materials: Preparations, Functionalities and Applications. *J. Mater. Chem. A* **2016**, *4* (10), 3584–3616. https://doi.org/10.1039/c5ta09924b.

(23) Zheng, Y.; Zheng, S.; Xue, H.; Pang, H. Metal-Organic Frameworks/Graphene-Based Materials: Preparations and Applications. *Adv. Funct. Mater.* **2018**, *28* (47), 1–28. https://doi.org/10.1002/adfm.201804950.

(24) Zhao, Y.; Cao, Y.; Zhong, Q. CO2 Capture on Metal-Organic Framework and Graphene Oxide Composite Using a High-Pressure Static Adsorption Apparatus. *J. Clean Energy Technol.* **2014**, *2* (1), 34–37. https://doi.org/10.7763/jocet.2014.v2.86.

(25) Al-Naddaf, Q.; Al-Mansour, M.; Thakkar, H.; Rezaei, F. MOF-GO Hybrid Nanocomposite Adsorbents for Methane Storage. *Ind. Eng. Chem. Res.* **2018**, *57* (51), 17470–17479. https://doi.org/10.1021/acs.iecr.8b03638.

(26) Liu, S.; Sun, L.; Xu, F.; Zhang, J.; Jiao, C.; Li, F.; Li, Z.; Wang, S.; Wang, Z.; Jiang, X.; Zhou, H.; Yang, L.; Schick, C. Nanosized Cu-MOFs Induced by Graphene Oxide and Enhanced Gas Storage Capacity. *Energy Environ. Sci.* **2013**, *6* (3), 818–823. https://doi.org/10.1039/c3ee23421e.

(27) Huang, W.; Zhou, X.; Xia, Q.; Peng, J.; Wang, H.; Li, Z. Preparation and Adsorption Performance of GrO@Cu-BTC for Separation of CO2/CH4. *Ind. Eng. Chem. Res.* **2014**, *53* (27), 11176–11184. https://doi.org/10.1021/ie501040s.

(28) Koh, H. S.; Rana, M. K.; Wong-Foy, A. G.; Siegel, D. J. Predicting Methane Storage in Open-Metal-Site Metal-Organic Frameworks. *J. Phys. Chem. C* **2015**, *119* (24), 13451–13458. https://doi.org/10.1021/acs.jpcc.5b02768.

(29) Rezaei, F.; Webley, P. Optimum Structured Adsorbents for Gas Separation Processes. *Chem. Eng. Sci.* **2009**, *64* (24), 5182–5191. https://doi.org/10.1016/j.ces.2009.08.029.

(30) Xin, C.; Zhan, H.; Huang, X.; Li, H.; Zhao, N.; Xiao, F.; Wei, W.; Sun, Y. Effect of Various Alkaline Agents on the Size and Morphology of Nano-Sized HKUST-1 for CO2 Adsorption. *RSC Adv.* **2015**, *5* (35), 27901–27911. https://doi.org/10.1039/c5ra03986j.

(31) Dąbrowski, A. Adsorption - From Theory to Practice. *Adv. Colloid Interface Sci.* **2001**, *93* (1–3), 135–224. https://doi.org/10.1016/S0001-8686(00)00082-8.

(32) Nuhnen, A.; Janiak, C. A Practical Guide to Calculate the Isosteric Heat/Enthalpy of Adsorption: Via Adsorption Isotherms in Metal-Organic Frameworks, MOFs. *Dalt. Trans.* **2020**, *49* (30), 10295–10307. https://doi.org/10.1039/d0dt01784a.

(33) Wang, X.; Ma, X.; Schwartz, V.; Clark, J. C.; Overbury, S. H.; Zhao, S.; Xu, X.; Song, C. A Solid Molecular Basket Sorbent for CO2 Capture from Gas Streams with Low CO2 Concentration under Ambient Conditions. *Phys. Chem. Chem. Phys.* **2012**, *14* (4), 1485–1492. https://doi.org/10.1039/c1cp23366a.

(34) Marcano, D. C.; Kosynkin, D. V.; Berlin, J. M.; Sinitskii, A.; Sun, Z.; Slesarev, A.; Alemany, L. B.; Lu, W.; Tour, J. M. Improved Synthesis of Graphene Oxide. *ACS Nano* **2010**, *4* (8), 4806–4814. https://doi.org/10.1021/nn1006368.

(35) Prestipino, C.; Regli, L.; Vitillo, J. G.; Bonino, F.; Damin, A.; Lamberti, C.; Zecchina, A.; Solari, P. L.; Kongshaug, K. O.; Bordiga, S. Local Structure of Framework Cu(II) in HKUST-1 Metallorganic Framework: Spectroscopic Characterization upon Activation and Interaction with Adsorbates. *Chem. Mater.* **2006**, *18* (5), 1337–1346. https://doi.org/10.1021/cm052191g.

(36) Alazmi, A.; Rasul, S.; Patole, S. P.; Costa, P. M. F. J. Comparative Study of Synthesis and Reduction Methods for Graphene Oxide. *Polyhedron* **2016**, *116*, 153–161. https://doi.org/10.1016/j.poly.2016.04.044.

(37) Thommes, M.; Kaneko, K.; Neimark, A. V.; Olivier, J. P.; Rodriguez-Reinoso, F.; Rouquerol, J.; Sing, K. S. W. Physisorption of Gases, with Special Reference to the Evaluation of Surface Area and Pore Size Distribution (IUPAC Technical Report). *Pure Appl. Chem.* **2015**, *87* (9–10), 1051–1069. https://doi.org/10.1515/pac-2014-1117.

(38) Jessop, P. G.; Hsiao, Y.; Ikariya, T.; Noyori, R. Homogeneous Catalysis in Supercritical Fluids: Hydrogenation of Supercritical Carbon Dioxide to Formic Acid, Alkyl Formates, and Formamides. *J. Am. Chem. Soc.* **1996**, *118* (2), 344–355. https://doi.org/10.1021/ja953097b.

(39) Huang, L.; Wang, H.; Chen, J.; Wang, Z.; Sun, J.; Zhao, D.; Yan, Y. Synthesis, Morphology Control, and Properties of Porous Metal-Organic Coordination Polymers. *Microporous Mesoporous Mater.* **2003**, *58* (2), 105–114. https://doi.org/10.1016/S1387-1811(02)00609-1.

(40) Santos, K. M. C.; Santos, R. J. O.; De Araújo Alves, M. M.; De Conto, J. F.; Borges, G. R.; Dariva, C.; Egues, S. M.; Santana, C. C.; Franceschi, E. Effect of High Pressure CO2 Sorption on the Stability of Metalorganic Framework MOF-177 at Different Temperatures. *J. Solid State Chem.* **2019**, *269* (October 2018), 320–327. https://doi.org/10.1016/j.jssc.2018.09.046.

(41) Vattipalli, V.; Qi, X.; Dauenhauer, P. J.; Fan, W. Long Walks in Hierarchical Porous Materials Due to Combined Surface and Configurational Diffusion. *Chem. Mater.* **2016**, *28* (21), 7852–7863. https://doi.org/10.1021/acs.chemmater.6b03308.

(42) Domán, A.; Czakkel, O.; Porcar, L.; Madarász, J.; Geissler, E.; László, K. Role of Water Molecules in the Decomposition of HKUST-1: Evidence from Adsorption, Thermoanalytical, X-Ray and Neutron Scattering Measurements. *Appl. Surf. Sci.* **2019**, *480* (February), 138–147. https://doi.org/10.1016/j.apsusc.2019.02.177.

(43) Sun, Y.; Ma, M.; Tang, B.; Li, S.; Jiang, L.; Sun, X.; Que, M.; Tao, C.; Wu, Z. Graphene Modified Cu-BTC with High Stability in Water and Controllable Selective Adsorption of Various Gases. *J. Alloys Compd.* **2019**, *808*, 151721. https://doi.org/10.1016/j.jallcom.2019.151721.

(44) Domán, A.; Klébert, S.; Madarász, J.; Sáfrán, G.; Wang, Y.; László, K. Graphene Oxide Protected Copper Benzene-1,3,5-Tricarboxylate for Clean Energy Gas Adsorption. *Nanomaterials* **2020**, *10* (6), 1–20. https://doi.org/10.3390/nano10061182.

(45) Kökçam-Demir, Ü.; Goldman, A.; Esrafili, L.; Gharib, M.; Morsali, A.; Weingart, O.; Janiak, C. Coordinatively Unsaturated Metal Sites (Open Metal Sites) in Metal-Organic Frameworks: Design and Applications. *Chem. Soc. Rev.* **2020**, *49* (9), 2751–2798. https://doi.org/10.1039/c9cs00609e.

(46) Supronowicz, B.; Mavrandonakis, A.; Heine, T. Interaction of Small Gases with the Unsaturated Metal Centers of the HKUST-1 Metal Organic Framework. *J. Phys. Chem. C* **2013**, *117* (28), 14570–14578. https://doi.org/10.1021/jp4018037.

(47) Rallapalli, P.; Prasanth, K. P.; Patil, D.; Somani, R. S.; Jasra, R. V.; Bajaj, H. C. Sorption Studies of CO2, CH4, N2, CO, O2 and Ar on Nanoporous Aluminum Terephthalate [MIL-53(Al)]. *J. Porous Mater.* **2011**, *18* (2), 205–210. https://doi.org/10.1007/s10934-010-9371-7.

(48) Makal, T. A.; Li, J. R.; Lu, W.; Zhou, H. C. Methane Storage in Advanced Porous Materials. *Chem. Soc. Rev.* **2012**, *41* (23), 7761–7779. https://doi.org/10.1039/c2cs35251f.

(49) Schoedel, A.; Ji, Z.; Yaghi, O. M. The Role of Metal–Organic Frameworks in a Carbon-Neutral Energy Cycle. *Nat. Energy* **2016**, *1* (4). https://doi.org/10.1038/nenergy.2016.34.

(50) Mason, J. A.; Veenstra, M.; Long, J. R. Evaluating Metal-Organic Frameworks for Natural Gas Storage. *Chem. Sci.* **2014**, *5* (1), 32–51. https://doi.org/10.1039/c3sc52633j.

(51) Tian, T.; Zeng, Z.; Vulpe, D.; Casco, M. E.; Divitini, G.; Midgley, P. A.; Silvestre-Albero, J.; Tan, J. C.; Moghadam, P. Z.; Fairen-Jimenez, D. A Sol-Gel Monolithic Metal-Organic Framework with Enhanced Methane Uptake. *Nat. Mater.* **2018**, *17* (2), 174–179. https://doi.org/10.1038/NMAT5050.

(52) Connolly, B. M.; Aragones-Anglada, M.; Gandara-Loe, J.; Danaf, N. A.; Lamb, D. C.; Mehta, J. P.; Vulpe, D.; Wuttke, S.; Silvestre-Albero, J.; Moghadam, P. Z.; Wheatley, A. E. H.; Fairen-Jimenez, D. Tuning Porosity in Macroscopic Monolithic Metal-Organic Frameworks for Exceptional Natural Gas Storage. *Nat. Commun.* **2019**, *10* (1), 1–11. https://doi.org/10.1038/s41467-019-10185-1.

(53) Peng, Y.; Krungleviciute, V.; Eryazici, I.; Hupp, J. T.; Farha, O. K.; Yildirim, T. Methane Storage in Metal-Organic Frameworks: Current Records, Surprise Findings, and Challenges. *J. Am. Chem. Soc.* **2013**, *135* (32), 11887–11894. https://doi.org/10.1021/ja4045289.

(54) López-Maya, E.; Montoro, C.; Colombo, V.; Barea, E.; Navarro, J. A. R. Improved CO2 Capture from Flue Gas by Basic Sites, Charge Gradients, and Missing Linker Defects on Nickel Face Cubic Centered MOFs. *Adv. Funct. Mater.* **2014**, *24* (39), 6130–6135. https://doi.org/10.1002/adfm.201400795.

(55) Hou, J.; Sapnik, A. F.; Bennett, T. D. Metal-Organic Framework Gels and Monoliths. *Chem. Sci.* **2020**, *11* (2), 310–323. https://doi.org/10.1039/c9sc04961d.

(56) Rezaei, F. *Optimization of Structured Adsorbents for Gas Separation Processes*; **2011**. Luleå University of Technology, Sweden. ISBN: 978-91-7439-233-3.

(57) Mallick, A.; Mouchaham, G.; Bhatt, P. M.; Liang, W.; Belmabkhout, Y.; Adil, K.; Jamal, A.; Eddaoudi, M. Advances in Shaping of Metal-Organic Frameworks for CO2 Capture: Understanding the Effect of Rubbery and Glassy Polymeric Binders. *Ind. Eng. Chem. Res.* **2018**, *57* (49), 16897–16902. https://doi.org/10.1021/acs.iecr.8b03937.

(58) Hong, W. Y.; Perera, S. P.; Burrows, A. D. Manufacturing of Metal-Organic Framework Monoliths and Their Application in CO2 Adsorption. *Microporous Mesoporous Mater.* **2015**, *214*, 149–155. https://doi.org/10.1016/j.micromeso.2015.05.014.

(59) Zhao, L.; Riensche, E.; Menzer, R.; Blum, L.; Stolten, D. A Parametric Study of CO2/N2 Gas Separation Membrane Processes for Post-Combustion Capture. *J. Memb. Sci.* **2008**, *325* (1), 284–294. https://doi.org/10.1016/j.memsci.2008.07.058.

(60) Bacsik, Z.; Cheung, O.; Vasiliev, P.; Hedin, N. Selective Separation of CO2 and CH4 for Biogas Upgrading on Zeolite NaKA and SAPO-56. *Appl. Energy* **2016**, *162*, 613–621. https://doi.org/10.1016/j.apenergy.2015.10.109.

(61) Pera-Titus, M. Porous Inorganic Membranes for CO2 Capture: Present and Prospects. *Chem. Rev.* **2014**, *114* (2), 1413–1492. https://doi.org/10.1021/cr400237k.

(62) Richardson, J. T.; Remue, D.; Hung, J. K. Properties of Ceramic Foam Catalyst Supports: Mass

and Heat Transfer. *Appl. Catal. A Gen.* **2003**, *250* (2), 319–329. https://doi.org/10.1016/S0926-860X(03)00287-4.

(63) Obaid, M.; Barakat, N. A. M.; Fadali, O. A.; Motlak, M.; Almajid, A. A.; Khalil, K. A. Effective and Reusable Oil/Water Separation Membranes Based on Modified Polysulfone Electrospun Nanofiber Mats. *Chem. Eng. J.* **2015**, *259*, 449–456. https://doi.org/10.1016/j.cej.2014.07.095.

For table of contents only